



HAL
open science

Consistency-based auto-calibration of the spectral model in dual-energy CT

J rome Lesaint, Simon Rit

► **To cite this version:**

J rome Lesaint, Simon Rit. Consistency-based auto-calibration of the spectral model in dual-energy CT. Seventh International Conference on Image Formation in X-Ray Computed Tomography, Jun 2022, Baltimore, United States. pp.47, 10.1117/12.2646526 . hal-03821856

HAL Id: hal-03821856

<https://hal.science/hal-03821856>

Submitted on 19 Oct 2022

HAL is a multi-disciplinary open access archive for the deposit and dissemination of scientific research documents, whether they are published or not. The documents may come from teaching and research institutions in France or abroad, or from public or private research centers.

L'archive ouverte pluridisciplinaire **HAL**, est destin e au d p t et   la diffusion de documents scientifiques de niveau recherche, publi s ou non,  manant des  tablissements d'enseignement et de recherche fran ais ou  trangers, des laboratoires publics ou priv s.

Consistency-based auto-calibration of the spectral model in dual-energy CT

Jérôme Lesaint^a and Simon Rit^b

^aUniv. Grenoble Alpes, CNRS, Grenoble INP, TIMC-IMAG,, 38000 Grenoble, France (e-mail : lesaint.jerome@gmail.com).

^bUniv. Lyon, INSA-Lyon, UCB Lyon 1, UJM-Saint Etienne, CNRS, Inserm, CREATIS UMR5220, U1206, Centre Léon Bérard, F-69373, Lyon, France.

ABSTRACT

We propose a consistency-based material decomposition algorithm. The method is free from any calibration procedure. The inverse spectral mixing model is approximated by a polynomial whose indeterminates are the raw-data values and whose coefficients are estimated by minimizing a consistency-based cost function. The consistency is in both the material sinograms and their mono-energetic combination. A small *a priori* on the object is incorporated in the minimization problem as a constraint. The method was evaluated on dual-energy simulations of a numerical phantom made of water and bone.

Keywords: Data consistency conditions (DCCs), spectral CT, material decomposition.

1. INTRODUCTION

This work is related to projection-domain material decomposition of energy-resolved X-ray projections, which aims to decompose energy-resolved projections onto a basis of material specific functions (Ref. 1). Since the early work of Alvarez and Macovski (Ref. 2), it is known that the linear attenuation coefficient μ can be modeled as a linear combination

$$\mu(\vec{x}, E) = \sum_{m=1}^M a_m(\vec{x}) f_m(E), \quad (1)$$

of a small number M of energy-dependent basis functions f_m . In Equation 1, f_m can for example be the linear attenuation of the material m (expressed in cm^{-1}) and $a_m(\vec{x})$ the unitless proportion of material m at spatial position \vec{x} . In typical photon-counting detectors, several photon counters are maintained at different energy ranges, based on pulse height analysis. We denote B the total number of energy bins. Each detector pixel returns B measurements m_b , modeled by the Beer-Lambert's law:

$$m_b = \int_0^\infty I_b^0(E) \exp\left(-\sum_{m=1}^M A_m f_m(E)\right) dE \quad (2)$$

where $I_b^0(E)$ is the effective spectrum of the bin b and $A_m = \int_{\mathcal{L}} a_m(\vec{x}) d\vec{x}$ is the line integral of the material map a_m along the X-ray path \mathcal{L} . In other words, A_m is the equivalent length of material m in the object μ along \mathcal{L} . In this work, the basis materials will be water and bone, so that $M = 2$ in the sequel.

By material decomposition, we mean recovering the coefficients A_m from the measurements m_b (or from their log s_b , see Equation 4 below). Several approaches have been proposed. A rigorous and natural way is to inverse the forward model $(m_1, \dots, m_B) = \Phi(A_1, \dots, A_m)$ of Equation 2. This has been done with a maximum likelihood approach in Ref. 3 further regularized in Ref. 4 or with a regularized least-square approach in Ref. 5. In all

This work was partially supported by grant ANR-17-CE19-0006 (ROI doré project) from the Agence Nationale de la Recherche (France). This work was performed within the framework of the SIRIC LYriCAN INCa-INSERM-DGOS-12563 and the LABEX PRIMES (ANR-11-LABX-0063) of Université de Lyon, within the program "Investissements d'Avenir" (ANR-11-IDEX-0007) operated by the French National Research Agency (ANR).

cases, the forward model needs to be known and the quality of the decomposition depends on the accuracy of the model. In particular, the effective spectra need to be calibrated, e.g. with a spectrometer for the source spectrum and monochromatic sources for the detector response. To avoid such a cumbersome procedure, it is possible to calibrate a parametric model either of the direct mapping Φ (Ref. 2) or of the inverse mapping $(A_1, \dots, A_M) = \Phi^{-1}(m_1, \dots, m_B)$ (or $\Phi^{-1}(s_1, \dots, s_B)$). In Ref. 6, the measured attenuations are related to the coefficients A_m via a polynomial model. The polynomial coefficients are learnt from a set of calibration measurements at various combinations of basis material lengths, which cover the range of length combinations that will be present in the imaged object. This procedure only requires a specific calibration phantom with known thicknesses of the basis materials but it is a time-consuming procedure. In Ref. 7, the authors introduce an empirical dual-energy material decomposition method. It is three-step: first, a calibration phantom, made of the basis materials, is scanned. Second, the reconstructed phantom image is segmented and regions of interest (ROI) of each material are selected. Third, the coefficients of a polynomial approximation of the inverse mapping Φ^{-1} are estimated so that the reconstruction obtained by applying the polynomial coefficients to the measures fits the segmented ROIs. The procedure is called *empirical* because the inverse mapping Φ^{-1} is indirectly estimated to retrieve the A_m from the m_b measurements without knowing I_b^0 .

The aim of the project is to avoid the calibration scan in the material decomposition. The polynomial coefficients of the inverse mapping are estimated by enforcing data consistency conditions on the material-specific sinograms. Consistency conditions have been successfully used in a number of CT artefacts correction problems, e.g., geometric calibration, beam-hardening correction, scatter correction. In this paper, we consider 2D parallel geometry only and its corresponding set of consistency conditions known as Helgason-Ludwig consistency conditions. The proposed method does not require a calibration scan, only the scan of the object of interest. The decomposition of the sinograms is exclusively based on the raw data, plus a tiny a priori knowledge on the object.

2. THEORY

The method minimizes a consistency-based cost function (subject to some constraints) which is described in this section. For simplicity, we focus on a 2D parallel scanning geometry. Projections are acquired over a 180 degree angular range. In a coordinate system (O, x, y) , we denote the projection angle θ (due to discretization, θ is assumed to vary in a set of discrete values Θ , whose cardinal is denoted $|\Theta|$) and the corresponding unit vector $\vec{\theta} = (\cos \theta, \sin \theta)$. The latter indicates the direction of the 1D linear detector, which is placed perpendicular to the direction of the X-rays. Position along the detector is denoted p (again, due to discretization, we denote δp the detector spacing and P the finite set of all pixel positions). Without loss of generality, we assume that the center of the detector is at the origin O of the coordinate system, that it rotates around O and that the object of interest fits the resulting field of view. At projection angle θ , the X-ray line $\mathcal{L}(\theta, p)$ intercepted at position p of the detector has equation $\vec{x} \cdot \vec{\theta} = p$.

2.1 Photon-counts and attenuations

Assuming a photon counting detector with B bins and according to Equation 2, the photon counts may be corrupted with Poisson noise. The measures become

$$m_b^*(\theta, p) \sim \text{Poisson}(m_b(\theta, p)). \quad (3)$$

We only use $m_b(\theta, p)$ in the rest of the paper and explicitly indicate whether data are corrupted with noise. The projections are then log-transformed according to

$$s_b(\theta, p) = -\log \left(\frac{m_b(\theta, p)}{m_{0,b}(\theta, p)} \right), \quad (4)$$

where $m_{0,b}$ is the number of photons without object.

2.2 The polynomial model

We look for a simplified model of the inverse mapping $(A_1, \dots, A_m) = \Phi^{-1}(s_1, \dots, s_B)$. We choose a polynomial model. Each material sinogram A_m is approximated by a polynomial $\psi_{m,D}$ of degree D in the variables (s_1, \dots, s_B) . Formally,

$$A_m \approx \psi_{m,D}(s_1, \dots, s_B) = \sum_{|k| \leq D} c_m^k s^k \quad (5)$$

where $k = (k_1, \dots, k_B)$ is a multi-index, $|k| = k_1 + \dots + k_B$ and $s^k = s_1^{k_1} \dots s_B^{k_B}$. We define $N(D, B)$ the total number of coefficients of a polynomial of degree D in B variables, e.g., $N(2,2)=6$ and $N(3,2)=10$. Note also that the coefficients c_m^k must be determined for each basis material m . If D, B and M are fixed, $M \times N(D, B)$ coefficients have to be determined. For example, if $B = 2, M = 2$ and $D = 3$, we seek $2 \times N(3, 2) = 20$ coefficients. Note that the same polynomial is applied to all the pixels of the sinogram A_m , i.e., that the source spectrum and the detector response are uniform over the beam and the detector, respectively.

2.3 The consistency metric

In 2D parallel geometry, the sought A_m are the Radon transform of the material map a_m

$$A_m(\theta, p) = \int_{\mathcal{L}(\theta, p)} a_m(\vec{x}) d\vec{x} = \int_{\mathbb{R}} a_m(p\vec{\theta} + q\vec{\theta}^\perp) dq \quad (6)$$

where $\vec{\theta} = (\cos \theta, \sin \theta)$ and $\vec{\theta}^\perp = (-\sin \theta, \cos \theta)$ are perpendicular.

To account for the spectral nature of the decomposition problem, we combine the material sinograms A_m into mono-energetic sinograms C_n , in view of applying the consistency metric to them. We choose N energy levels E_n in the energy range of the source and form the mono-energetic sinograms C_n

$$C_n(\theta, p) = \sum_{m=1}^M f_m(E_n) A_m(\theta, p). \quad (7)$$

The coefficients $f_m(E_n)$ are known (see [Equation 1](#)).

A consistency condition of the Radon transform states that the integral of each projection (the order-0 moment) does not depend on the projection angle θ since each of these integrals equals the integral of the attenuation coefficient over the object. We define the moment $J_n(\theta)$ of the C_n by

$$J_n(\theta) = \int_{\mathbb{R}} C_n(\theta, p) dp = \sum_{n=1}^N f_m(E_n) \int_{\mathbb{R}} A_m(\theta, p) dp \quad (8)$$

We use the variance of J_n to evaluate if J_n is constant over Θ . The consistency function hence reads:

$$\ell_n(\mathbf{c}) = \frac{1}{|\Theta|} \sum_{\theta \in \Theta} (J_n(\theta) - \overline{J_n(\theta)})^2 \quad (9)$$

where $\overline{J_n(\theta)}$ denotes the mean of J_n over all θ . Note that the function ℓ_n depends on the polynomial coefficients $\mathbf{c} = (c_m^k)$ since all A_m do (see [Equation 5](#)). Finally, we define M consistency functions $\ell'_m(\mathbf{c})$ on the material sinograms A_m in a similar way. The final consistency metric accumulates the consistency of all computed mono-energetic sinograms and all material-specific sinograms

$$\ell(\mathbf{c}) = \sum_{n=1}^N \ell_n(\mathbf{c}) + \sum_{m=1}^M \ell'_m(\mathbf{c}) \quad (10)$$

The consistency metric would evaluate to zero on perfectly consistent material sinograms.

2.4 Minimization

Due to the hardening of the beam in each bin (see e.g. Ref. 8), the measured attenuations s_b do not satisfy the consistency condition. The loss ℓ is minimized with respect to the coefficients \mathbf{c} to achieve mono-energetic and material sinograms which are as consistent as possible.

Since we use only order-0 consistency conditions, a constant sinogram (i.e. $A_m(\theta, p) = \text{constant}$ for all θ and p) is perfectly consistent. To prevent the minimization to output such undesirable solution, we follow the idea of Ref. 8 and constrain the minimization by some known values. First, if there is no attenuation in all bins ($s_b = 0, \forall b \in \{1, \dots, B\}$), we enforce 0 in all material and mono-energetic sinograms by setting $c_m^0 = 0$ for all m . Second, there still is a trivial solution to the minimization of the consistency loss function: the null sinogram. We enforce, for each material m , a particular value in one voxel of each reconstructed material map a_m . To this end, a small sample of each material is placed in the field-of-view and a reconstruction from raw data is computed. The small samples are easily identifiable in the reconstruction. Let \vec{x}_m be one voxel in each material sample and assume reconstructions are computed with a standard Filtered Backprojection (FBP) algorithm. Since FBP is a linear operation, one has

$$a_m(\vec{x}_m) = \text{FBP} \left(\sum_{|k| \leq d} c_m^k s^k \right) (\vec{x}_m) = \sum_{|k| \leq d} c_m^k \text{FBP}(s^k)(\vec{x}_m). \quad (11)$$

The values $\text{FBP}(s^k)(\vec{x}_m)$ are easily computed once, before the minimization. Each material map is constrained by exactly M relations, which take the form

$$\sum_{|k| \leq d} c_m^k \text{FBP}(s^k)(\vec{x}_{m'}) = \begin{cases} 0 & \text{if } m \neq m' \\ 1 & \text{if } m = m' \end{cases} \quad (12)$$

3. NUMERICAL EXPERIMENTS

3.1 Simulation of data

Numerical experiments used a 2D phantom made of an outer water disc of diameter 32 mm and five bone inserts (with diameters ranging from 2 to 5 mm), placed inside the water disc (see Figure 2). Two tiny inserts of bone and water (1 mm in diameter each) were placed outside the phantom. One voxel in each insert was chosen for the constraints. The material sinograms A_m were analytically computed with RTK (Ref. 9). The simulated sinograms had 700 pixels with 0.05 mm spacing and 720 projections over a 180° angular range. Two effective spectra were used. The low-energy (LE) and high-energy (HE) spectra had a tube-voltage of 80 keV and 120 keV respectively (Figure 1). Without object, the detector received a total number of photons of 1.3×10^6 and 2.9×10^6 photons for the LE and HE spectra respectively. The photon counts m_b were computed by applying Equation 2, then log-transformed according to Equation 4.

The degree of the sought polynomials was fixed to $D = 3$ and the consistency metric Equation 10 was minimized under the constraints defined above, with the Sequential Least Squares Programming algorithm. The total number of estimated polynomial coefficients was 18. The initial guess was always set to zero for all coefficients.

3.2 Evaluation methods

Our method was compared to the calibration from a set of dedicated measurements with the same LE and HE spectra over a set of water and bone lengths. The set covered all combinations which were present in the phantom. More precisely, 100 equi-spaced lengths of each material were measured. Water lengths ranged from 0 to 32.6 mm and bone lengths ranged from 0 to 10.97 mm. All these combinations were irradiated with the same LE and HI spectra as the phantom. Then the polynomials $\tilde{\psi}_{m,D}$ were fitted to the calibration data and further applied to the phantom data to produce a reference polynomial decomposition.

We compared the poly-energetic reconstructions from raw-data with mono-energetic images computed from our DCC-based material maps and from the reference calibrated material maps.

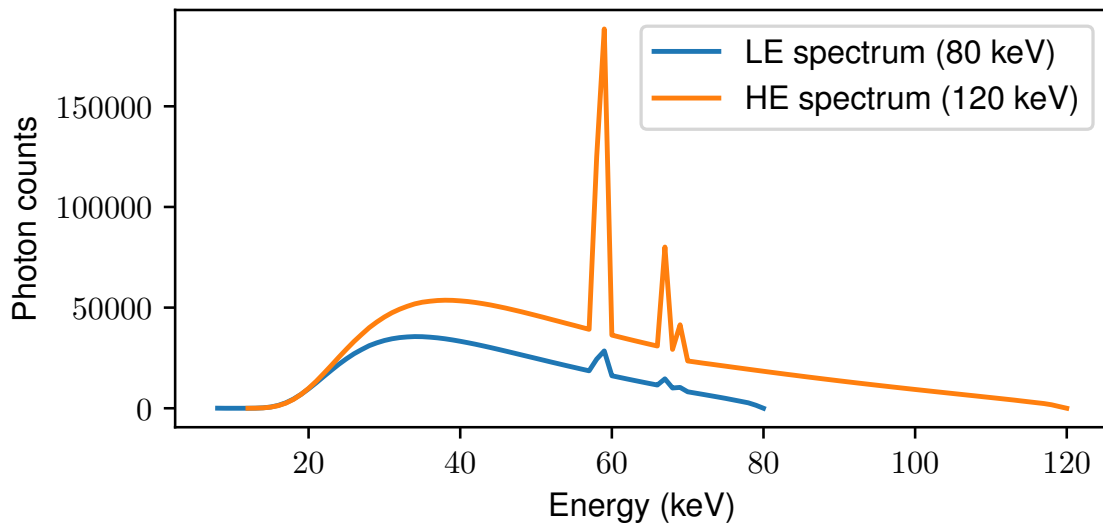


Figure 1. The low-energy (LE) and high-energy (HE) spectra.

4. RESULTS

4.1 Noise-less data

Results of the decomposition are shown in Figure 2. Water and bone are adequately separated. The profiles in Figure 2 (bottom row) indicate residual cross-talk between the two material maps. In the center of the water phantom, the low-contrast feature is visible.

Since the consistency is enforced on the mono-energetic images, Figure 3 compares poly-energetic images, DCC-based and calibration-based mono-energetic images. Poly-energetic images clearly suffer from severe beam-hardening, which is almost completely corrected on both mono-energetic images. The profiles presented in Figure 4 reveal that the DCC-based and calibrated 40 keV images can hardly be distinguished. A slight discrepancy between the 80 keV images still subsists though, especially in the vicinity of the border of the phantom.

4.2 Robustness to noise

The photons count measurements m_b were corrupted with Poisson noise according to Equation 3. The reference photon flux is given by the spectra in Figure 1, i.e. 1.3×10^6 and 2.9×10^6 photons for the LE and HE spectra respectively. The noise level was set by reducing the total number of emitted photons by a factor 1, 10 and 100. The influence of noise on the material maps is presented in Figure 5. The quality of the images is significantly degraded. The consistency function value at convergence increases with the level of noise. It is 0.2108 for reference noise level (factor 1), 1.4738 at factor 10 and 12.815 at factor 100. We expect the choice of the reference voxel to play a critical role in the presence of heavy noise.

5. DISCUSSION AND CONCLUSION

We have demonstrated a consistency-based material decomposition, which does not require any calibration procedure. Only the raw data and a tiny *a priori* knowledge on the object are sufficient to produce material specific sinograms. This tiny *a priori* can be implemented in practice by placing inserts in the field-of-view of the scanner. The resulting sinograms are free from beam-hardening. The method achieves (on simulated data) results that are close to those obtained with a standard calibration-based decomposition method.

The influence of the choice of the reference voxels in the reconstruction may play a critical role and should be further investigated. By choosing a voxel in the reconstruction as a reference, we indirectly incorporate in the constraint all the projections values from lines passing through the voxel (with filtered back-projection, all

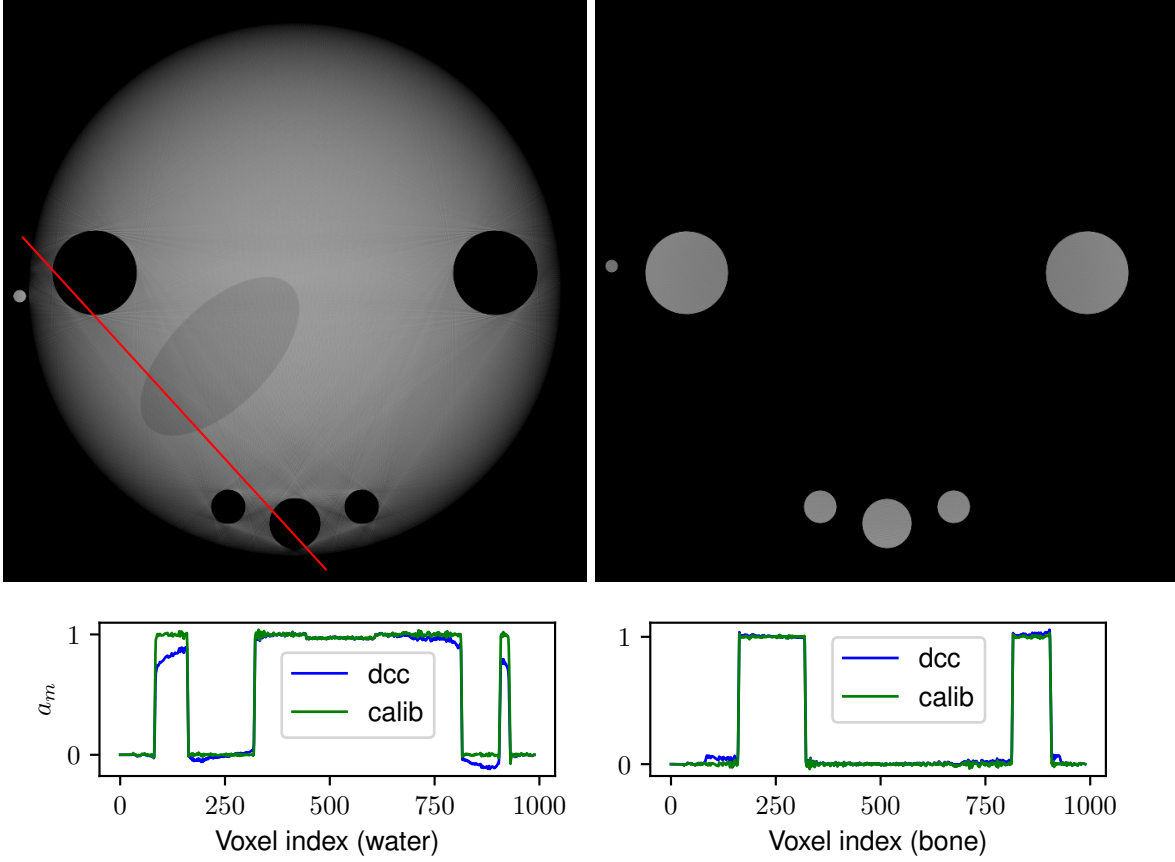


Figure 2. *Top*: Material map obtained with the DCC-based decomposition. Grayscale is : 1 ± 0.3 . The red line indicates the profile used in Figure 4. *Bottom*: Profiles along the red line for the DCC-based and the calibrated water (*left*) and bone (*right*) maps. The consistency metric at convergence was $\ell(c) = 0.0208$. If evaluated on the calibrated sinograms, the consistency function was 0.0018.

the lines are incorporated but the ramp filter drops rapidly, so mainly the lines through the voxel are). If those lines “see” a wider range of length combinations, we expect that the decomposition is improved.

Finally, we used a parallel geometry for its simplicity. But order-0 DCC are also available for divergent beam 3D data. In Ref. 8, they use such DCC to correct beam-hardening in a circular acquisition. We expect that the decomposition method presented in this work generalizes to multi-energy divergent projections.

REFERENCES

- [1] Rit, S., Mory, C., and Noël, P., “Image Formation in Spectral Computed Tomography,” in [*Spectral, Photon Counting Computed Tomography*], 355–372, CRC Press (jul 2020).
- [2] Alvarez, R. E. and Macovski, A., “Energy-selective reconstructions in X-ray computerized tomography.,” *Physics in medicine and biology* **21**(5), 733–44 (1976).
- [3] Roessl, E. and Proksa, R., “K-edge imaging in x-ray computed tomography using multi-bin photon counting detectors,” *Physics in Medicine and Biology* (2007).
- [4] Brendel, Bernhard and Bergner, Frank and Brown, Kevin and Koehler, T., “Penalized likelihood decomposition for dual layer spectral CT,” in [*Proc 4th intl mtg on image formation in X-ray CT*], 41—4 (2016).
- [5] Ducros, N., Abascal, J. F. P.-J., Sixou, B., Rit, S., and Peyrin, F., “Regularization of nonlinear decomposition of spectral x-ray projection images,” *Medical Physics* **44**, e174–e187 (sep 2017).

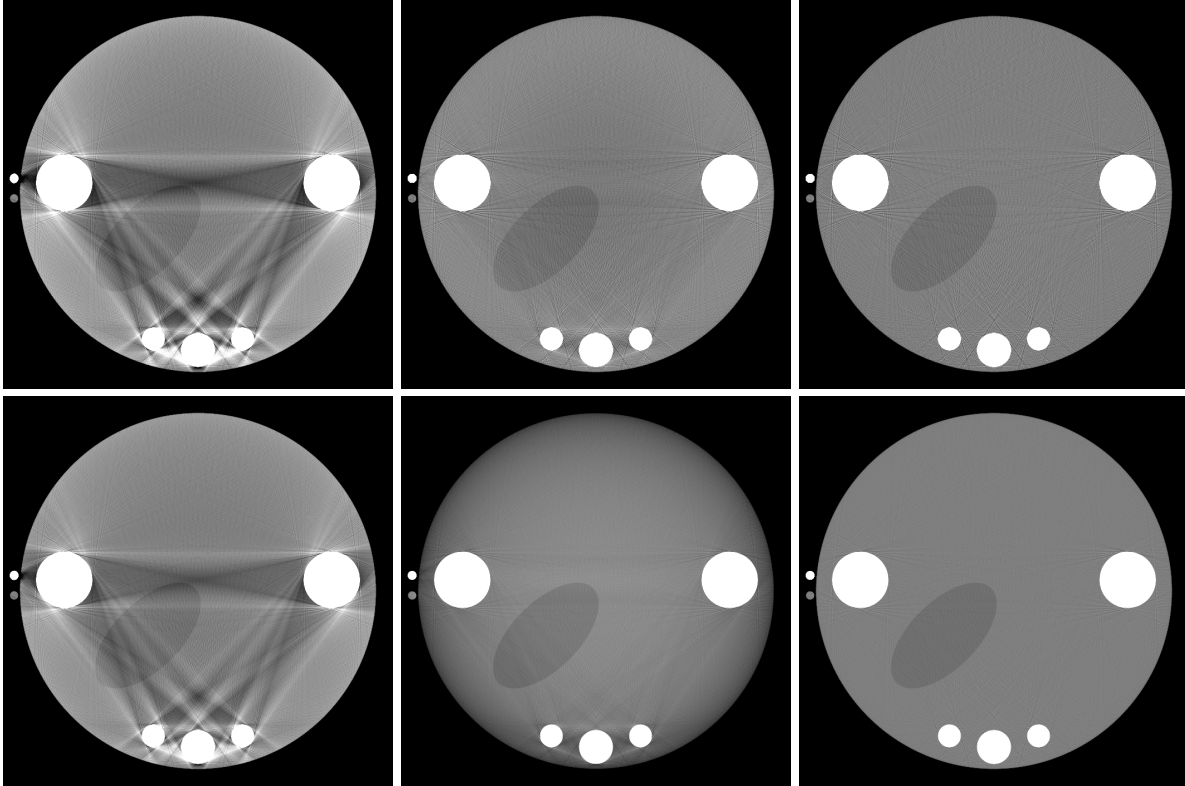


Figure 3. Poly-energetic reconstructions (*left*) from LE (*top*) and HE (*bottom*) data. DCC-based (*middle*) and calibration-based (*right*) mono-energetic images at 40 keV (*top*) and 80 keV (*bottom*). Grayscale for all images : $0 \pm 250\text{HU}$.

- [6] Alvarez, R. E., “Estimator for photon counting energy selective x-ray imaging with multibin pulse height analysis,” *Medical Physics* (2011).
- [7] Stenner, P., Berkus, T., and Kachelriess, M., “Empirical dual energy calibration (EDEC) for cone-beam computed tomography,” *Medical Physics* **34**, 3630–3641 (aug 2007).
- [8] Würfl, T., Maaß, N., Dennerlein, F., Huang, X., and Maier, A. K., “Epipolar Consistency Guided Beam Hardening Reduction-ECC 2,” in [*14th International Meeting on Fully Three-Dimensional Image Reconstruction in Radiology and Nuclear Medicine*], 181–185 (2017).
- [9] Rit, S., Oliva, M. V., Brousmiche, S., Labarbe, R., Sarrut, D., and Sharp, G. C., “The Reconstruction Toolkit (RTK), an open-source cone-beam CT reconstruction toolkit based on the Insight Toolkit (ITK),” *Journal of Physics: Conference Series* **489**(1), 12079 (2014).

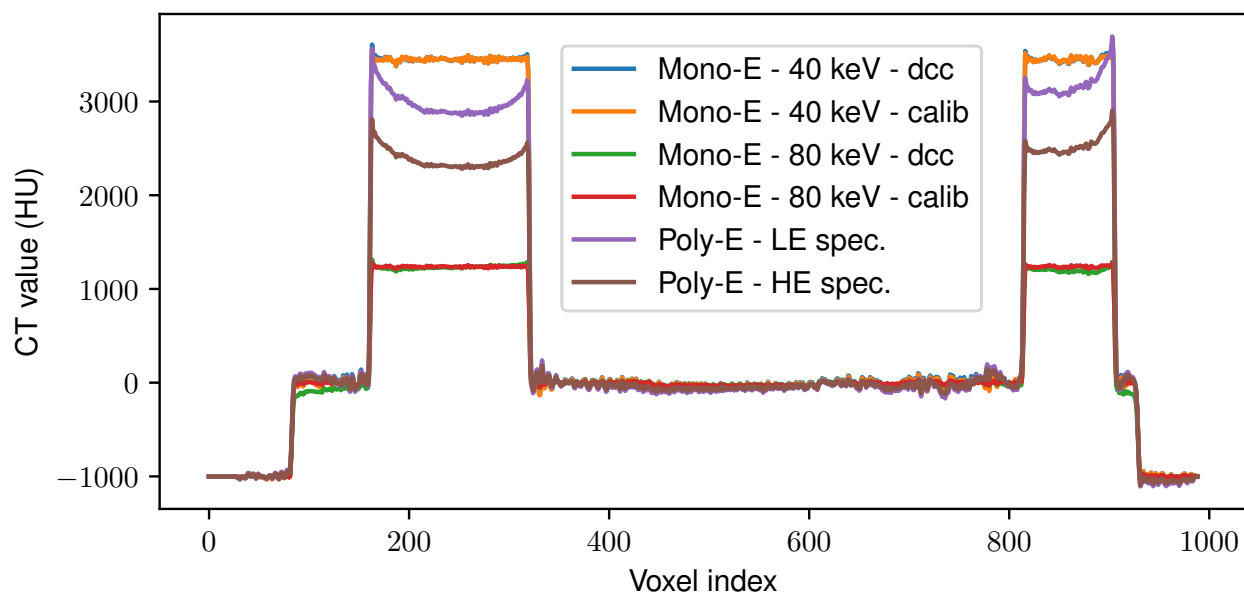


Figure 4. Profile poly-energetic reconstructions from raw data and from mono-energetic images computed from DCC-based and calibrated material maps.

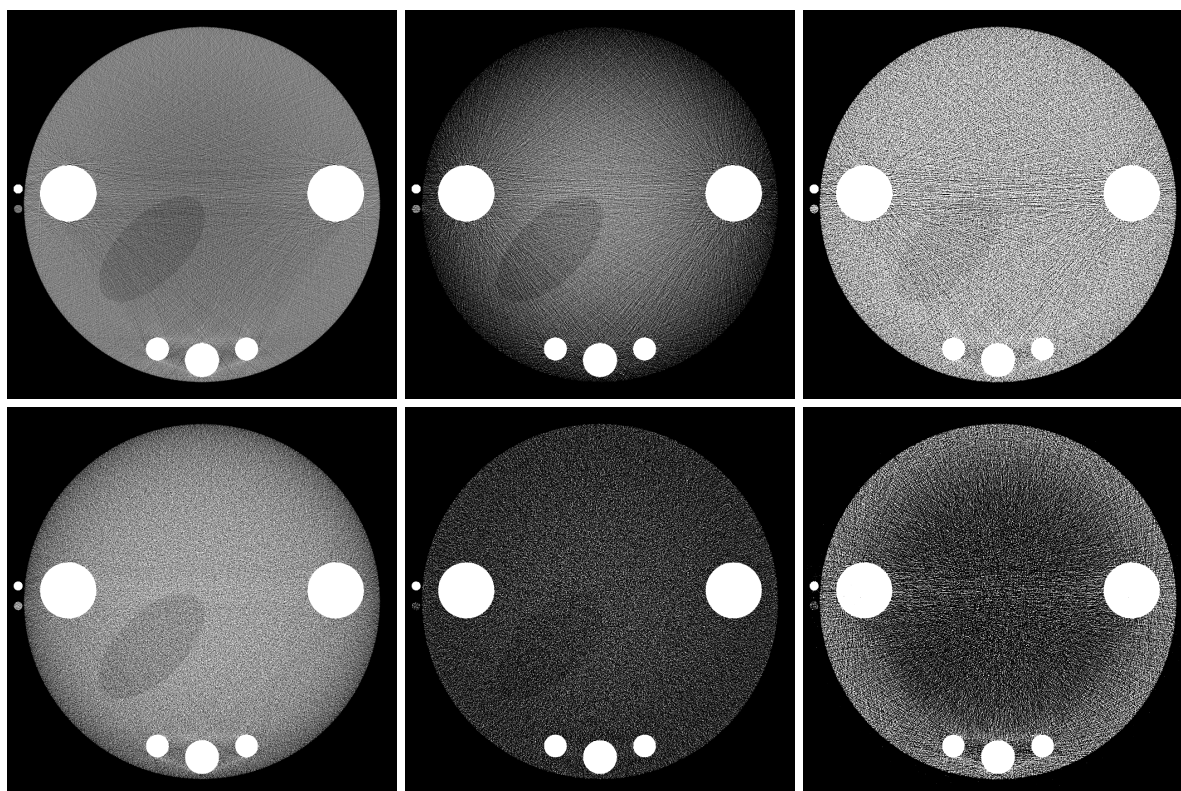


Figure 5. Mono-energetic images at 40 keV (*top*) and 80 keV (*bottom*), for Poisson noise with photon counts downscaled by a factor 1, 10 and 100 (from *left to right*). Grayscale for all images : $0 \pm 250\text{HU}$. The consistency function at convergence was $\ell(\mathbf{c}) = 0.2108, 1.4738, 12.815$ for factor 1, 10 and 100 respectively.